Article

Investigation of WO₃ and BiVO₄ Photoanodes for Photoelectrochemical Sensing of Xylene, Toluene and Methanol

Milda Petruleviciene [1] [iD], **Irena Savickaja** [1] [iD], **Jurga Juodkazyte** [1] [iD] **and Arunas Ramanavicius** [1,2,*] [iD]

1   Centre for Physical Sciences and Technology, Sauletekio Av. 3, 10257 Vilnius, Lithuania; milda.petruleviciene@ftmc.lt (M.P.); irena.savickaja@ftmc.lt (I.S.); jurga.juodkazyte@ftmc.lt (J.J.)
2   Department of Physical Chemistry, Faculty of Chemistry, Vilnius University, 03225 Vilnius, Lithuania
*   Correspondence: arunas.ramanavicius@chf.vu.lt; Tel.: +370-(60)-032332; Fax: +370-(52)-469210

Abstract: Volatile organic compounds (VOCs) are a notable group of indoor air pollutants released by household products. These substances are commonly employed as solvents in industrial operations, and some of them are recognized or suspected to be cancer-causing or mutagenic agents. Due to their high volatility, VOCs are typically present in surface waters at concentrations below a few micrograms per liter. However, in groundwater, their concentrations can reach levels up to thousands of times higher. This study analyses the applicability of the photoelectrochemical (PEC) sensing of VOCs in aqueous medium. Tungsten oxide and bismuth vanadate photoanodes were tested for PEC sensing of xylene, toluene, and methanol in sodium chloride and sodium sulfate electrolytes. The crystalline structure and morphology of coatings were analyzed using XRD and SEM analyses. Photoelectrochemical properties were evaluated using cyclic voltammetry, chronoamperometry, and electrochemical impedance spectroscopy. The results of the study show that aromatic compounds tend to block the surface of the photoelectrode and interfere with the PEC sensing of other substances. WO₃ photoanode is found to be suitable for the PEC sensing of methanol under the mild conditions in aqueous electrolytes; however, electrode engineering and assay optimization are required to achieve better detection limits.

Keywords: photoelectrochemistry; volatile organic compounds; photoanode; tungsten oxide; bismuth vanadate; detection

1. Introduction

Industry and household products release a significant group of indoor air pollutants known as volatile organic compounds. VOCs are found in a wide range of products, from fuels, solvents, paints, adhesives, and deodorants to refrigerants. They are also found in the emissions resulting from combustion processes, with trihalomethanes being particularly prevalent in chlorinated drinking water. The release of VOCs into the environment occurs throughout their entire lifecycle, including production, distribution, storage, handling, and use. This leads to their potential entry into both surface water and groundwater supplies through various point and nonpoint sources [1]. VOCs include different alcohols, aromatics (such as benzene, toluene, and xylene), aldehydes, and halocarbons [2,3]. In addition to their tendency to accumulate and persist in the environment, VOCs contribute to the greenhouse effect and the resulting depletion of the ozone layer. Due to their impact on the environment and human health, the detection of VOCs has been gaining increasing attention recently [4–7]. In relatively unpolluted waters, VOCs account for about 10% of total dissolved organic carbon, and their levels are particularly elevated in untreated waters of various anthropogenic origins. The most popular technique for the detection of VOCs is gas chromatography (GC); however, it requires time-consuming sample preparation procedures, such as solvent extraction, gas-phase extraction, purge and trap capillary or membrane extraction [8,9]. Furthermore, there has been a growing interest in the

employment of photocatalytic oxidation, an environmentally friendly and energy-efficient advanced oxidation technique, to degrade pollutants [4]. There are several studies in which tungsten oxide, titanium oxide, and zinc oxide semiconductors were applied as gas sensors for the detection of VOCs [10–14]. In these studies, the limits of detection for xylene and toluene ranged between 10 and 100 ppm depending on the modification of photoanodes [14–18]; however, in these studies, high temperatures of 200–400 °C were used for detection, requiring sophisticated equipment and high energy input. The mentioned studies were focused on the detection of VOCs in the gas phase, whereas the number of studies on the determination of VOCs in aqueous medium is very limited.

Photoelectrochemical systems can be applied to the sensing and detection of various organic compounds [18–20]. PEC sensing has several advantages, such as sensitivity, fast analysis time, and low detection limit [21,22]. The efficiency of the sensing strongly depends on the nature of the photoelectrode, the electrolytes, and the illumination conditions, etc. Semiconductors differ in positions of valence and conduction bands, which determine whether photoinduced charge carriers have sufficient energy to carry out certain oxidation-reduction reactions. For an efficient performance, photoelectrodes must be able to absorb wide range of visible light and be stable in a specific range of pH (for practical use, preferably, in a neutral pH). Recently, there has been growing interest in tungsten oxide and bismuth vanadate [23–26]. These two semiconductors exhibit distinct characteristics, including different stabilities within specific pH ranges and different energies of photoinduced holes (~3 eV for WO_3 and ~2.4 eV for $BiVO_4$) [27–30]. They also differ in the lifetime of the photogenerated carriers and the diffusion length of the holes (~150 nm for WO_3 and ~80 nm for $BiVO_4$), resulting in different performances of these photoanodes [31,32].

This work presents the comparative study on the application of WO_3 and $BiVO_4$ semiconductors for the PEC sensing of xylene, toluene, and methanol in aqueous NaCl and Na_2SO_4 electrolytes. Methanol was chosen as a representative of a different class of organic compounds in order to compare how the nature of VOCs influences PEC sensing performance. The crystalline structure and morphology of the synthesized coatings were analyzed using XRD and SEM analyses. Photoelectrochemical experiments were conducted using cyclic voltammetry (CV), electrochemical impedance spectroscopy (EIS), and chronoamperometry (CA) techniques. The results show that aromatic compounds tend to block the photoelectrode surface, leading to an inverse proportionality between the amount of VOC and the photocurrent. Only the WO_3/Na_2SO_4 system was found to be suitable for the detection of xylene with LOD ~3.25 mg L^{-1}. In the case of methanol, the direct proportionality between the photocurrent and concentration of VOC was found and the best sensing performance was demonstrated by WO_3/NaCl with an LOD of 16.5 mg L^{-1}. The applicability of PEC sensing for VOCs in aqueous medium was evaluated for the first time.

2. Materials and Methods

2.1. Materials and Reagents

All chemicals used in this study were of analytical grade. Sodium tungstate dihydrate ($Na_2WO_4 2H_2O$) (Carl Roth, Karlsruhe, Germany), ammonium oxalate (($NH_4)_2C_2O_4$) (Chempur, Piekary, Slaskie), hydrochloric acid (HCl) (Chempur, Piekary, Slaskie), hydrogen peroxide (H_2O_2) (Chempur, Piekary, Slaskie), methanol (CH_3OH) (Reachem, Bratislava, Slovakia), isopropanol (C_3H_7OH) (Reachem, Bratislava, Slovakia), bismuth pentahydrate ($Bi(NO_3)_3 \times 5H_2O$) (Carl Roth (Karlsruhe, Germany)), ammonium vanadate (NH_4VO_3) (Acros Organics, Kandel, Germany), nitric acid (HNO_3) (Chempur, Piekary, Slaskie), polyvinyl alcohol ((PVA) (Chempur, Piekary, Slaskie), ammonium molybdate heptahydrate (($NH_4)_6Mo_7O_{24} \times 7H_2O$) (Chempur, Piekary, Slaskie), xylene (C_8H_{10}) (mixture of isomers) (Reachem, Bratislava, Slovakia), and toluene (C_7H_8) (Lachner, Neratovice, Czech Republic) were used as received from suppliers without further purification.

2.2. Synthesis of Tungsten Oxide and Bismuth Vanadate

WO_3 thin films were fabricated on fluorine-doped tin oxide (FTO) substrates following a slightly modified procedure outlined in detail in [33,34]. The FTO substrates with a resistance of 5–7 Ω/sq were cut into 1×2.5 cm^2 slides and were ultrasonically cleaned in acetone, isopropanol, and deionized water for 15 min in each. A solution of $Na_2WO_4 \times 2H_2O$ and $(NH_4)_2C_2O_4$ in deionized water was prepared, and HCl was added while continuously stirring at 40 °C. Subsequently, H_2O_2 was added to form peroxotungstic acid, followed by the addition of isopropanol (IsoPrOH) as a reductant. After 10 min, the cleaned conducting glass substrates were immersed in the prepared mixture with the FTO side facing down and kept for 140 min. The deposition process was carried out at a constant temperature of 85 °C in a water bath. The coated slides were then rinsed in distilled water for 1 min and dried in a drying oven at 40 °C for 10 h. Finally, the coatings were annealed in ambient atmosphere at 400 °C for 2 h, with a heating rate of 1 °C min^{-1} and a starting temperature of 20 °C.

$BiVO_4$ coatings were synthesized through a sol-gel process as detailed in reference [35]. Initially, 2.94 g of $Bi(NO_3)_3 \times 5H_2O$ and 0.702 g of NH_4VO_3, with a molar ratio of 1:1, were dissolved in 23% HNO_3. Subsequently, 2.52 g of citric acid ($C_6H_8O_7$) was added under continuous stirring, resulting in the formation of a transparent blue solution. To adjust the viscosity of the sol-gel, 1 g of polyvinyl alcohol (PVA) and 3 mL of acetic acid were introduced. After 4 h of mixing, 0.702 g of $(NH_4)_6Mo_7O_{24} \times 7H_2O$, corresponding to 10 atomic percent of Mo, was added to the solution, and the resulting mixture was stirred overnight (12 h) on a magnetic stirrer at 20 °C. The obtained sol-gel was then utilized for the deposition of thin films on FTO substrates. The FTO slides were prepared using the same method as in the synthesis of tungsten oxide. The procedure for dip-coating was conducted with a dip-coater (Nadetech, ND-DC 11/1) at an immersing and pulling rate of 100 mm/min, lasting for 60 s. After the deposition, the layers were annealed in air at 450 °C (with a heating rate of 1 °C min^{-1}) to achieve crystalline Mo-doped $BiVO_4$ coatings. The deposition process was repeated twice.

2.3. Structural and Morphological Analysis of WO$_3$ and BiVO$_4$

The crystalline structure of the WO_3 and $BiVO_4$ coatings was examined using an X-ray diffractometer, specifically the SmartLab system (Rigaku), which was equipped with a 9 kW rotating Cu anode X-ray tube. The analysis was conducted within a 2θ range of 20–80° using the grazing incidence (GIXRD) method, where a 0.5° angle (ω) was set between a parallel beam of X-rays and the surface of the specimen. To identify the phases present, the Match software was used in conjunction with the Crystallography Open Database (COD). The surface morphology of the prepared samples was investigated using the Helios NanoLab dual beam workstation, manufactured by Oxford Instruments in the Netherlands.

2.4. Photoelectrochemical Investigations

Cyclic voltammetry (CV) and electrochemical impedance spectroscopy (EIS) measurements were carried out in a three-electrode electrochemical cell using potentiostat/galvanostat Zennium/Zahner Xpot (Zahner Elektrik, Kronach-Gundelsdorf, Germany). Experiments were performed in 0.5 M Na_2SO_4 (Acros Organics (Kandel, Germany) using WO_3 and $BiVO_4$ coatings on FTO substrates as working electrodes. Ag/AgCl$_{(sat. KCl)}$ and Pt plate (1×1 cm^2) were used as reference and counter electrodes, respectively. All reported potential values in the paper are referenced against Ag/AgCl$_{(sat. KCl)}$. The surface of the working electrodes was illuminated using a high-intensity discharge Xe-lamp with a spectrum of 6000 K. The lamp was calibrated using a silicon diode to simulate AM 1.5 illumination at an intensity of approximately 100 mW cm^{-2}. Nyquist plots were measured at a potential of 0.7 V with an AC amplitude of 10 mV within a frequency range of 10^4 to 0.1 Hz under illumination.

Applied bias photon-to-current efficiency (ABPE, %) measurements were performed in a two-electrode cell using WO_3 or $BiVO_4$ coatings and Pt plate as working and counter electrodes, respectively. Linear sweep measurements were performed at a 50 mV s^{-1} scan rate in 0.5 M Na_2SO_4. ABPE (%) was calculated using equation:

$$ABPE\ (\%) = \frac{I_{ph}(E_0 - E_{bias})}{P} \times 100\%, \tag{1}$$

where I_{ph} is photocurrent (mA cm^{-2}), E_0 is the thermodynamic potential of a reaction (V), E_{bias} is the applied bias (V), and P is the power of illumination. In our experiments, E_0 was 2.4 V, considering that the anodic process is $SO_4^{2-} \rightarrow S_2O_8^{2-}$ with E^0 = 2.0 V (SHE) [36] and the cathodic one is a hydrogen evolution reaction with E^0 = −0.413 V (SHE) at pH 7; the power of illumination corresponded to 1 sun (~100 mW cm^{-2}).

Chronoamperometry (CA) under chopped illumination was performed in a two-electrode cell at 1.4 V bias (vs. Pt) using WO_3 and $BiVO_4$ photoanodes as working electrodes and a Pt counter electrode. Experiments were performed in 0.5 M NaCl and 0.5 M Na_2SO_4 electrolytes. Further, for the evaluation of sensing, experiments under chopped illumination were performed in 0.1 M NaCl and 0.1 M Na_2SO_4 electrolytes containing 1, 5, and 10 mg L^{-1} of xylene, 1, 5, and 10 mg L^{-1} of toluene, and 50, 100, and 250 mg L^{-1} of methanol. To prevent potential contamination of the photoelectrode surface, new samples of WO_3 and $BiVO_4$ were employed for every test.

The production of reactive sulfate species (RSS) and reactive chlorine species (RCS) was investigated in the two-electrode setup in the solutions of 0.5 M Na_2SO_4 and 0.5 M NaCl, respectively. Photoelectrolysis was performed under an applied bias of 1.4 V (vs. Pt) until the charge of ~1 C had passed through the system. After that, the electrolyte from the anodic compartment of the cell was collected and the presence of RSS in the form of $S_2O_8^{2-}$ and RCS in the form of $ClO^- + ClO_2^-$ was investigated by means of chromatometric and iodometric titration, respectively. The theoretic amount of RCS and RSS, m_{theor}, was calculated according to Faraday's law on the basis of an electric charge, Q (C), passed through the cell during photoelectrolysis assuming 2-electron transfer in the oxidation of SO_4^{2-} to $S_2O_8^{2-}$ and Cl^- to ClO^-. The Faradaic efficiency, FE (%), of the photoelectrochemical generation of RCS and RSS was evaluated as the ratio $m_{exp}/m_{theor} \times 100$. Titration protocols for the determination of persulfate and chlorine species are described in detail in our previous works [35,37,38].

3. Results and Discussion

3.1. Structural and Morphological Characterisation of WO_3 and $BiVO_4$ Coatings

Figure 1 displays the X-ray diffraction (XRD) patterns of tungsten oxide (Figure 1a) and bismuth vanadate (Figure 1b) coatings. The diffractograms exhibit distinct peaks corresponding to the crystalline structure of tungsten oxide (indicated as asterisks) and bismuth vanadate (indicated as diamonds), as verified by the COD database entries 2311041 and 9013436, respectively. Additionally, the spectrum of $BiVO_4$ sample reveals peaks attributable to the FTO substrate (indicated by circles).

The morphology of WO_3 and $BiVO_4$ coatings was evaluated using SEM (Figure 1c,d). The tungsten oxide layer is composed of randomly oriented plates with a size range of approximately 500 to 2200 nm, whereas the bismuth vanadate coating consists of fused elongated and rounded particles, ranging in size from about 10 to 50 nm, forming a film-like structure.
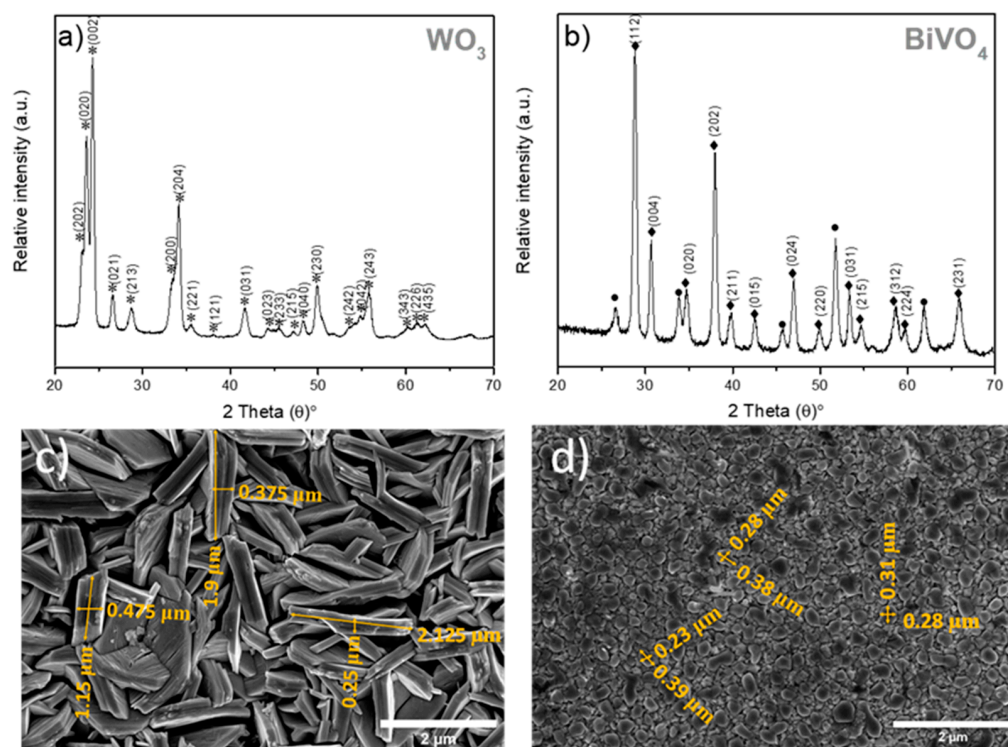
Figure 1. XRD patterns (**a**,**b**) and SEM images (**c**,**d**) of WO_3 (**a**,**c**) and $BiVO_4$ (**b**,**d**) coatings. Peak symbols: *—WO_3 (COD data base No: 2311041), ♦—$BiVO_4$ (COD data base No: 9013436), •—SnO_2 (COD data base No: 9009082).

3.2. Photoelectrochemical Characterization of WO_3 and $BiVO_4$ Coatings

The photoelectrochemical properties of WO_3 and $BiVO_4$ coatings were evaluated using cyclic voltammetry and electrochemical impedance spectroscopy techniques. From the CVs shown in Figure 2a, it can be seen that the photocurrent in both cases starts to rise when E exceeds 0.3 V. Nevertheless, in the case of tungsten oxide, this increase is sharper and, at about 0.7 V, the current stabilizes and remains steady for the remaining potential range. As for bismuth vanadate, the photocurrent rises steadily across the entire potential range, reaching a value of approximately 0.9 mA cm^{-2} at 1.6 V, which is about two times higher than the I_{ph} of tungsten oxide at the same E. The steeper increase of I_{ph} observed in the case of WO_3 may indicate a lesser extent of charge carrier recombination, because a higher applied bias is required for $BiVO_4$ to facilitate charge separation and achieve the same magnitude of photocurrent. The saturation of the photocurrent observed in the case of WO_3 indicates that the maximum rate of interfacial charge transfer has been reached under the specific conditions of the experiment, whereas for $BiVO_4$, such a limit was not attained. The charge transfer resistances (R_{ct}) of the synthesized coatings as determined by EIS were ~5000 Ω for WO_3 and almost four times lower for $BiVO_4$, i.e., 1200 Ω (Figure 2b). Figure 2c illustrates that the ABPE values for both coatings are remarkably similar, with a maximum value of approximately 0.2%. The peak of WO_3 is slightly shifted to the lower voltage values, indicating that a slightly lower potential is required to achieve the highest efficiency of light to electric energy conversion.

In Figure 3a,b chronoamperograms of tungsten oxide and bismuth vanadate coatings, recorded under chopped illumination in 0.5 M NaCl and 0.5 M Na_2SO_4, are presented. The key distinction between the two photoelectrodes lies in the shape of the curves: the initial photocurrent spikes were more pronounced in the case of bismuth vanadate photoanode. This phenomenon again indicates that, upon illumination, a substantial concentration of charge carriers is excited; however, due to rapid recombination processes, the photocurrent decreases rapidly until reaching a stationary state.
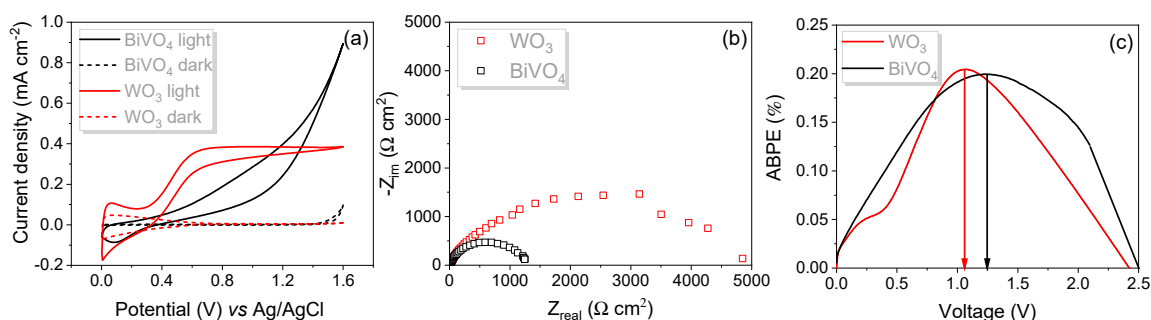
Figure 2. CVs of tungsten oxide and bismuth vanadate coatings recorded at 50 mV s^{-1} scan rate (**a**), Nyquist plots recorded at 0.7 V within a frequency range from 10^4 to 0.1 Hz under illumination (**b**) and ABPE plots (**c**); all measurements were performed in 0.5 M Na$_2$SO$_4$.
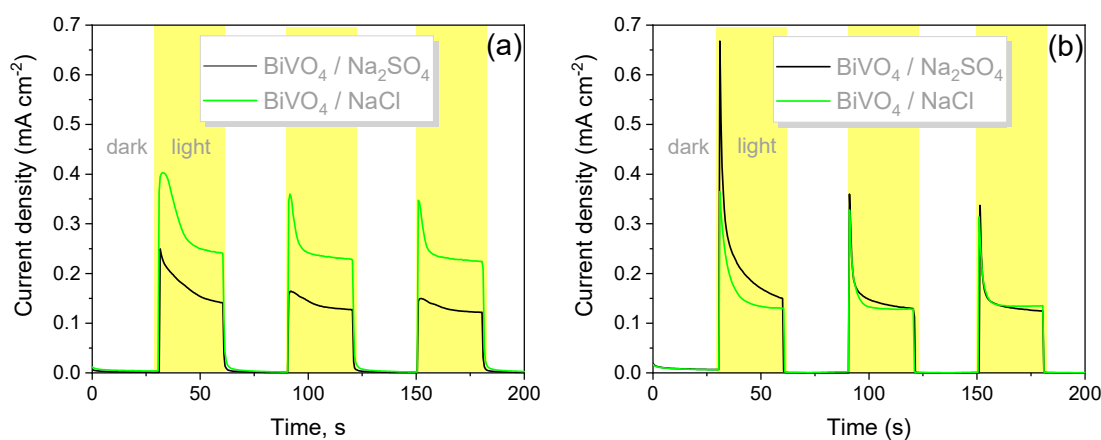

Figure 3. Chronoamperograms of WO$_3$ (**a**) and BiVO$_4$ (**b**) coatings recorded under chopped light illumination in 0.5 M NaCl and 0.5 M Na$_2$SO$_4$ electrolytes at 1.4 V (vs. Pt).

The highest quasi-stationary photocurrent was achieved for WO$_3$ in NaCl electrolyte (Figure 3a). A contrasting trend was observed with the BiVO$_4$ coating. Initially, the highest I$_{ph}$ was obtained in sodium sulfate solution but, as the experiment progressed, the photocurrents in both electrolytes became comparable.

Such differences in photoresponse could be related to different thermodynamics as well as kinetics of photoelectrochemical reactions on the photoanode surface. Different thermodynamics refer to different valence band positions, hence different energies of photoinduced holes in the studied semiconductors. From the literature, it is known that the energy of photoinduced holes (h$^+$) in tungsten oxide and bismuth vanadate corresponds to ~3 V and ~2.4 V vs. SHE, respectively [29,38]. Due to different energetics, holes have different abilities to oxidize the solution species. In fact, holes have enough energy to oxidize water and dissolved anions to reactive radical species, e.g., E^0(OH•/H$_2$O) = 2.31 V (SHE) at pH 7) [39], E^0(Cl•/Cl$^-$) = 2.432 V (SHE) [40,41] and E^0(SO$_4$•/SO$_4^{2-}$) = 2.437 V (SHE) [40,42], which can further participate in various photochemical reactions with molecules and ions present in the supporting electrolyte [43,44]. The competition between the photoanodic oxidation of water and anions is influenced by the affinity of certain species to adsorb on the photoelectrode's surface because those ions or molecules, which are adsorbed on the surface, would have a kinetic advantage over the others in the process of hole scavenging. The adsorption is, in turn, influenced by the pH of the electrolyte, the surface charge, and also the morphology of the coatings [38].

The photoanodic formation of reactive chlorine species (ClO$^-$ + ClO$_2^-$) and reactive sulfate species (S$_2$O$_8^{2-}$) in 0.5 M NaCl and 0.5 M Na$_2$SO$_4$ electrolytes was confirmed by means of a titrimetric analysis of the oxidation products after the passage of 1 C in a PEC cell using WO$_3$ and BiVO$_4$ photoelectrodes. The results are presented in Figure 4.

Faradaic efficiencies of RCS and RSS formation in the case of $BiVO_4$ were ~81% and ~71%, respectively, whereas for tungsten oxide, FE values were somewhat lower: ~75% and ~61%. FE values below 100% most likely indicate that the remaining part of the photogenerated charge is consumed during the production of hydrogen peroxide and/or oxygen.
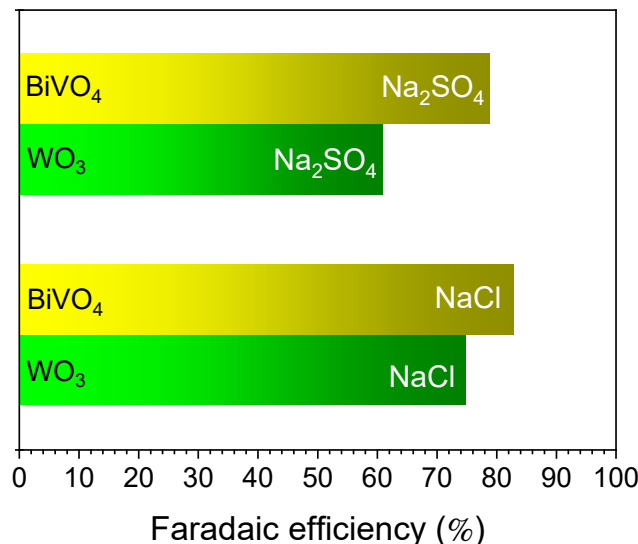

Figure 4. Comparison of Faradaic efficiencies (%) of photoelectrochemically produced RCS and RSS using WO_3 and $BiVO_4$ photoanodes in 0.5 M NaCl and 0.5 M Na_2SO_4 electrolytes.

3.3. PEC Detection of Xylene with WO_3 and $BiVO_4$ Photoanodes

Next, WO_3 and $BiVO_4$ coatings were tested in the photoelectrochemical sensing of xylene, toluene, and methanol in 0.1 M NaCl and 0.1 M Na_2SO_4 electrolytes. Methanol (MeOH) was chosen to compare how the nature of the organic compound influences the sensing performance. It should also be noted that MeOH has much higher hydrophilicity in comparison with xylene and toluene. In these experiments, 0.1 M solutions were used to reduce the ionic strength of the electrolytes, resulting in better solubility of xylene and toluene. Chronoamperograms of WO_3 and $BiVO_4$ photoelectrodes recorded under chopped illumination in 0.1 M NaCl and 0.1 M Na_2SO_4, with or without 1, 5, and 10 mg L^{-1} of xylene or toluene and 50, 100, and 250 mg L^{-1} of methanol, are shown in Figures S1 and S2 in the supporting information. Figure 5 displays the correlation between the VOC concentration and the ratio I_{ph}/I_0, where I_{ph} and I_0 refer to the quasi-stationary photocurrents, which were measured at the end of the second illumination period in the electrolyte with and without the analyte, respectively (Figures S1 and S2). It can be seen that I_{ph}/I_0 mostly decreased with the increase in concentrations of xylene and toluene in both electrolytes for both photoanodes (Figures S1a–d and S2a–d), whereas a random response was observed in the cases of $BiVO_4/Na_2SO_4$ with xylene and WO_3/Na_2SO_4 with toluene (Figure 5a,b). Such behavior implies that presence of these aromatic compounds somehow interfered with charge transfer reactions occurring at the photoelectrode/electrolyte interface. When xylene was used as the analyte (Figure 5a), the slower decrease of the photocurrent was observed for WO_3 in both electrolytes as compared to $BiVO_4$, implying that the interference of xylene with competing photoanodic reactions (formation of RCS and RSS) was more significant in the case of $BiVO_4$. A completely different situation was, however, observed with methanol, where the photocurrent as well as I_{ph}/I_0 increased with the amount of MeOH in the case of WO_3 and $BiVO_4$ coatings in both electrolytes, except for $BiVO_4/Na_2SO_4$, where the photocurrent was independent of the methanol concentration (Figure 5c, Figures S1e,f and S2e,f). The results of the PEC sensing performance presented in Figure 5 are summarized in Table 1, where calculated regression equations with correlation coefficients and limits of detection (LOD) are listed. It is evident that photoelectrochemical sensing is strongly influenced by the nature of photoanodes, analytes, and electrolytes. WO_3 demonstrated

a linear decrease of I_{ph} with increasing xylene concentration in the range of 0–10 mgL^{-1} with a 3.25 mg L^{-1} LOD in Na$_2$SO$_4$ electrolyte with a signal-to-noise ratio of 3. However, in NaCl electrolyte, WO$_3$ and BiVO$_4$ did not show good linear dependence. In the case of toluene (0–10 mg L^{-1}), a rather wide scattering of experimental points was obtained for all investigated PEC systems: the addition of the lowest amount of toluene was enough to suppress the I_{ph} to a certain level, which was almost not influenced by the increase in amount of the analyte (Figure 5b). With methanol, linear dependences with correlation coefficients of 0.99733 and 0.98764 and LODs of 16.5 mg L^{-1} and 33.76 mg L^{-1} were obtained for WO$_3$/NaCl and WO$_3$/Na$_2$SO$_4$ coatings, respectively. For the BiVO$_4$ coating, linear dependence was observed only in the sodium chloride electrolyte with a correlation coefficient of 0.96099 and an LOD of 64.39 mg L^{-1}.
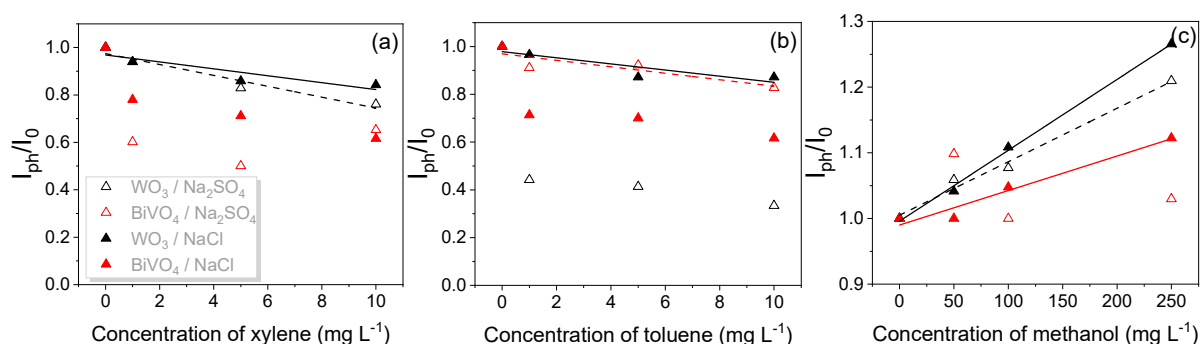

Figure 5. Ratio of I_{ph} and I_0 obtained from chopped light illumination experiments vs. concentration of xylene (**a**), toluene (**b**), and methanol (**c**) for WO$_3$ and BiVO$_4$ photoelectrodes in 0.1 M NaCl and 0.1 M Na$_2$SO$_4$ electrolytes.

Table 1. Regression equations with correlation coefficients and limits of detection (LODs) of WO$_3$ and BiVO$_4$ photoanodes.

VOC	PEC System	The Regression Equation I_{ph}/I_0 = Slope × C (mg L^{-1}) + Intercept	Correlation Coefficient	LOD mg L^{-1}
Xylene	WO$_3$/NaCl	$-0.01284C + 0.9776$	0.81585	6.22
Xylene	WO$_3$/Na$_2$SO$_4$	$-0.0229C + 0.97418$	0.94192	3.25
Xylene	BiVO$_4$/NaCl	$-0.03115C + 0.90151$	0.753	7.5
Toluene	WO$_3$/NaCl	$-0.01284C + 0.9776$	0.7885	6.77
Toluene	WO$_3$/Na$_2$SO$_4$	$-0.04693C + 0.73532$	0.48905	13.39
Toluene	BiVO$_4$/NaCl	$-0.02808C + 0.86992$	0.58283	11.08
Toluene	BiVO$_4$/Na$_2$SO$_4$	$-0.01356C + 0.96963$	0.77057	7.14
Methanol	WO$_3$/NaCl	$0.00108C + 0.99595$	0.99733	16.5
Methanol	WO$_3$/Na$_2$SO$_4$	$8.14033 \times 10^{-4}C + 1.00499$	0.98764	35.76
Methanol	BiVO$_4$/NaCl	$5.2535 \times 10^{-4}C + 0.99002$	0.96099	64.39

Photoelectrochemical sensing in the case of n-type semiconductors is based on the interaction between photoinduced holes and solution species, leading to the generation of a photocurrent, whereas photoexcited electrons from the conduction band are transferred to the cathode to participate in reduction reactions. The same mechanism applies for the PEC degradation of organic compounds. In certain cases, photoelectrons can be scavenged by ions or molecules adsorbed on the photoanode's surface, which results in the reduction of the net current flowing through the cell. Such a scenario was recently reported in [45], where the effect of dopamine on the PEC performance of BiVO$_4$/FeOOH was studied. There are two potential explanations for the observed decrease in I_{ph} when xylene or toluene is added: either it adsorbs onto the semiconductor's surface, creating a physical barrier that restricts the access of other solution species that can be oxidized by holes, or it functions as a photoelectron acceptor, thus decreasing the net photocurrent. Xylene and toluene molecules have a benzene ring, which could act as an effective electron acceptor and inhibit electron transfer from the photoactive coating to the FTO substrate [46,47]. Methanol, on the contrary, does not block the surface of the photoanode and actively

participates in hole scavenging, leading to an increase in I_{ph}. Due to its low oxidation potential ($E^0(CH_3OH/CH_3O^{\bullet})$ = 0.48 V vs. SHE [48]), the ability of methanol to undergo photooxidation is well known and has been investigated in numerous PEC systems involving various semiconductors, e.g., TiO_2, ZnO, Fe_2O_3, CdS, $BiVO_4$, and WO_3 [48–51]. PEC formation of formaldehyde with 96% Faradaic efficiency was found to take place on an α-Fe_2O_3 photoanode in 95% CH_3OH + 0.1 M NaOH [49]. The mechanism is believed to proceed via methoxy radical formation:

$$CH_3OH + h^+ \rightarrow CH_3O\bullet + H^+ \qquad\qquad (2)$$

$$CH_3O\cdot + h^+ \rightarrow CH_2O + H^+. \qquad\qquad (3)$$
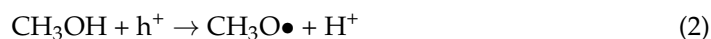
In more dilute methanol solutions, such as those investigated in this study, as well as in the presence of other dissolved species (Cl^-, SO_4^{2-}), competition between the photoanodic processes and possible interactions between the photogenerated species may play an important role in determining the composition of the products of PEC processes [52,53]. The fact that the valence band edge of WO_3 is deeper than that of $BiVO_4$ can explain the faster response and higher linearity obtained for the WO_3 photoelectrode in methanol sensing (Table 1), because the holes in WO_3 have a greater energy offset to drive the CH_3OH oxidation reaction. There are several studies in which cysteine-stabilized Cd quantum dots or TiO_2 have been used for the PEC detection of methanol and LODs were 0.16 mg L^{-1} [54] and 0.24 mg L^{-1} [55], respectively. PEC sensing of xylene and toluene was mostly applied for gas phase samples, where high temperatures were required. Only a few studies report the electrochemical (i.e., not light-assisted) detection of xylene and toluene in aqueous phase using a boron-doped diamond or glassy carbon-supported $ZnO/MgO/Cr_2O_3$ nanofiber anodes, respectively [56,57]. The reported LODs for detection of xylene and toluene were 0.0954 mg L^{-1} and 0.0736 mg L^{-1}, respectively. The LODs obtained in our study are higher, indicating the need to optimize the photoanodes as well as the measurement conditions.

The interaction of photoinduced holes with an analyte may be direct or indirect. In the latter case, dissolved organic compounds are degraded via reactions with photogenerated oxidizing species. In [4,47,49], an electron spin resonance (ESR) analysis was applied to demonstrate that xylene and other organic compounds adsorbed on the surface of TiO_2 or ZnO are mainly degraded by hydroxyl and superoxide radicals, produced by the PEC oxidation of water molecules. It is also known that methanol is a good scavenger of $OH\bullet$ [58]. However, RCS and RSS can also actively participate in the degradation of organic compounds [59–62]. The formation of these species has also been evidenced by ESR [43,63–68], though the intensity of the signals in the ESR spectra was lower compared to those of $OH\bullet$. The latter fact implies that the formation of RCS and RSS can also be induced by $OH\bullet$ [44,64,69]. Possible mechanisms of RCS and RSS formation were discussed in our previous studies [35,37]. The fact that VOCs' sensing performance of WO_3 and $BiVO_4$ photoelectrodes depends on the electrolyte can be explained by competing interactions occurring between photogenerated holes, reactive chlorine, sulfate or oxygen species, and VOCs. These complex photo(electro)chemical equilibria are strongly influenced by the nature of the photoelectrode (i.e., energy of holes) as well as by the morphology of the surface.

As previously mentioned, the reduction in photocurrents observed in electrolytes containing xylene or toluene implies that these aromatic compounds, owing to their high lipophilicity, have the ability to passivate the surface of the photoanode. This was confirmed through chronoamperometric experiments in which xylene, toluene, and methanol were sequentially introduced to the 0.1 M NaCl electrolyte containing 50 mg L^{-1} of xylene, while monitoring the photocurrent (Figure 6). The amounts of analytes added dropwise in the close vicinity of the electrode surface were as follows: 100 μL of 100 mg L^{-1} xylene, 50 μL of 200 mg L^{-1} toluene, and 50 μL of 500 mg L^{-1} methanol. It is evident that neither WO_3 nor $BiVO_4$ exhibited any response in I_{ph} regardless of the added analytes. This proves that aromatic compounds tend to block the surface of the photoelectrode,

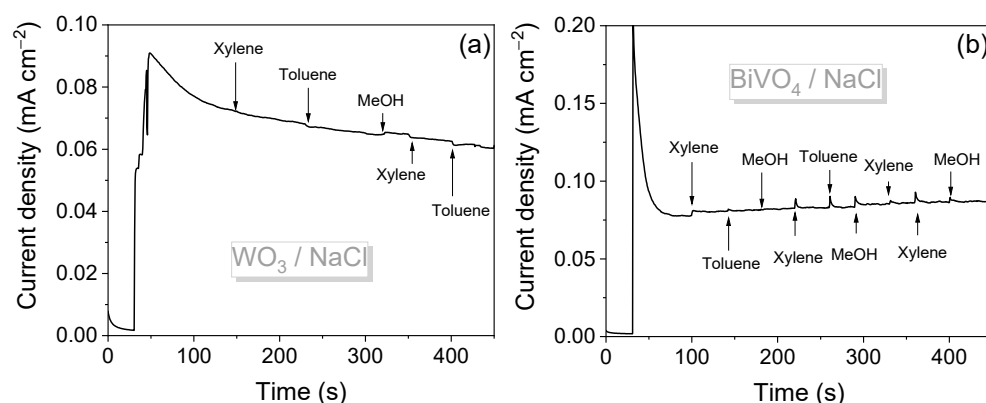preventing photoinduced hole transfer reactions and thus interfering with the PEC sensing of other analytes.

Figure 6. Effect of addition of 100 μL of 100 mg L^{-1} xylene, 50 μL of 200 mg L^{-1} toluene, and 50 μL of 500 mg L^{-1} methanol on photocurrent of WO$_3$ (**a**) and BiVO$_4$ (**b**) photoelectrodes in 0.1 M NaCl containing 50 mg L^{-1} xylene under applied bias of 1.4 V (vs. Pt).

4. Conclusions

In this work, a comparative analysis of the photoelectrochemical sensing of VOCs—namely xylene, toluene, and methanol—using WO$_3$ and BiVO$_4$ photoanodes in aqueous solutions of NaCl and Na$_2$SO$_4$ was carried out. Semiconductor layers were synthesized using a sol-gel route. Both coatings demonstrated high photoelectrochemical activity. The charge transfer resistance (R$_{ct}$) of the coatings, determined by EIS, was approximately 5000 Ω for WO$_3$ and 1200 Ω for BiVO$_4$. Maximum ABPE values for both coatings found in the sodium sulfate electrolyte were around 0.2%.

It was found that an increase in the concentration of the studied aromatic VOCs, i.e., xylene and toluene, leads to a decrease in the photocurrent. This behavior was explained either by the electrode surface blocking it due to the adsorption of these compounds, which prevents the interaction of photogenerated holes with solution species, or by photoelectron scavenging by the adsorbed aromatic molecules. The best sensitivity to xylene in the studied concentration range of 0–10 mg L^{-1} was found for WO$_3$/Na$_2$SO$_4$, with a limit of detection of 3.25 mg L^{-1}. No reliable linear correlation was obtained for toluene in all the PEC systems studied. In the case of methanol, direct proportionality between the concentration of alcohol and the photocurrent was found in all PEC systems except for BiVO$_4$/Na$_2$SO$_4$. The determined LODs for WO$_3$/NaCl and WO$_3$/Na$_2$SO$_4$ were 16.5 mg L^{-1} and 33.76 mg L^{-1}, respectively. In the case of BiVO$_4$/NaCl, the LOD for methanol was 64.39 mg L^{-1}.

The findings of this study demonstrate that a tungsten oxide photoanode is suitable for the photoelectrochemical sensing of methanol under the mild conditions in aqueous electrolytes. However, electrode engineering and assay optimization are required to achieve better detection limits. The BiVO$_4$ coatings produced in this study were found to be unsuitable for the PEC sensing of xylene, toluene, and methanol, presumably due to the fast contamination of the surface and the strong influence of competing PEC processes, i.e., the oxidation of other solution species. The latter process is most likely influenced by the energy of photogenerated holes and the morphology of the photoelectrode surface. It has been shown that aromatic compounds tend to block the surface of the photoelectrode, hindering photoinduced charge transfer reactions and thus interfering with the PEC sensing of other compounds.

Supplementary Materials: The following supporting information can be downloaded at: https:// www.mdpi.com/article/10.3390/chemosensors11110552/s1, Figure S1: Chronoamperograms of WO_3 (a,c,e) and $BiVO_4$ (b,d,f) photoanodes in 0.1 M NaCl electrolyte with and w/o xylene, toluene and methanol; chopped illumination, 1.4 V (vs. Pt). Figure S2: Chronoamperograms of WO_3 (a,c,e) and $BiVO_4$ (b,d,f) photoanodes in 0.1 M Na_2SO_4 electrolyte with and w/o xylene, toluene and methanol; chopped illumination, 1.4 V (vs. Pt).

Institutional Review Board Statement: Not applicable.

Informed Consent Statement: Not applicable.

Data Availability Statement: The data presented in this study are available on request from the corresponding author.

Conflicts of Interest: The authors declare no conflict of interest.

References

1. Golfinopoulos, S.K.; Lekkas, T.D.; Nikolaou, A.D. Comparison of methods for determination of volatile organic compounds in drinking water. *Chemosphere* **2001**, *45*, 275–284. [CrossRef]
2. Lloyd, A.C.; Cackette, T.A. Diesel Engines: Environmental Impact and Control. *J. Air Waste Manag. Assoc.* **2001**, *51*, 809–847. [CrossRef]
3. Akhtar, N.; Syakir Ishak, M.I.; Bhawani, S.A.; Umar, K. Various natural and anthropogenic factors responsible for water quality degradation: A review. *Water* **2021**, *13*, 2660. [CrossRef]
4. Wang, Z.; Xie, X.; Wang, X.; Mahmood, A.; Qiu, H.; Sun, J. Difference of photodegradation characteristics between single and mixed VOC pollutants under simulated sunlight irradiation. *J. Photochem. Photobiol. A Chem.* **2019**, *384*, 112029. [CrossRef]
5. Morin, J.; Brochard, G.; Bergé, V.; Rosset, A.; Artous, S.; Clavaguera, S.; Strekowski, R.S.; Wortham, H. Uptake of m-xylene and VOC emissions by mineral photocatalytic paints of indoor air building interest. *Environ. Sci. Nano* **2023**, *10*, 1704–1714. [CrossRef]
6. Beauchet, R.; Mijoin, J.; Batonneau-Gener, I.; Magnoux, P. Catalytic oxidation of VOCs on NaX zeolite: Mixture effect with isopropanol and o-xylene. *Appl. Catal. B Environ.* **2010**, *100*, 91–96. [CrossRef]
7. Jayawardhana, Y.; Gunatilake, S.R.; Mahatantila, K.; Ginige, M.P.; Vithanage, M. Sorptive removal of toluene and m-xylene by municipal solid waste biochar: Simultaneous municipal solid waste management and remediation of volatile organic compounds. *J. Environ. Manag.* **2019**, *238*, 323–330. [CrossRef]
8. Chary, N.S.; Fernandez-Alba, A.R. Determination of volatile organic compounds in drinking and environmental waters. *TrAC Trends Anal. Chem.* **2012**, *32*, 60–75. [CrossRef]
9. Nikolaou, A.D.; Golfinopoulos, S.K.; Kostopoulou, M.N.; Kolokythas, G.A.; Lekkas, T.D. Determination of volatile organic compounds in surface waters and treated wastewater in Greece. *Water Res.* **2002**, *36*, 2883–2890. [CrossRef]
10. Sumitsawan, S.; Cho, J.; Sattler, M.L.; Timmons, R.B. Plasma surface modified TiO_2 nanoparticles: Improved photocatalytic oxidation of gaseous m-xylene. *Environ. Sci. Technol.* **2011**, *45*, 6970–6977. [CrossRef]
11. Liu, W.; Wei, D.; Zhao, X.; Xiao, F.; Yang, C. Enhanced xylene-sensing property of hierarchical NiO/montmorillonite hetero-structures via in doping. *Appl. Surf. Sci.* **2022**, *602*, 154301. [CrossRef]
12. Li, F.; Qin, Q.; Zhang, N.; Chen, C.; Sun, L.; Liu, X.; Chen, Y.; Li, C.; Ruan, S. Improved gas sensing performance with Pd-doped $WO_3 \cdot H_2O$ nanomaterials for the detection of xylene. *Sens. Actuators B Chem.* **2017**, *244*, 837–848. [CrossRef]
13. Gao, H.; Yu, Q.; Chen, K.; Sun, P.; Liu, F.; Yan, X.; Liu, F.; Lu, G. Ultrasensitive gas sensor based on hollow tungsten trioxide-nickel oxide (WO_3-NiO) nanoflowers for fast and selective xylene detection. *J. Colloid Interface Sci.* **2019**, *535*, 458–468. [CrossRef] [PubMed]
14. Kang, Y.; Kim, K.; Cho, B.; Kwak, Y.; Kim, J. Highly Sensitive Detection of Benzene, Toluene, and Xylene Based on CoPP-Functionalized TiO_2 Nanoparticles with Low Power Consumption. *ACS Sens.* **2020**, *5*, 754–763. [CrossRef] [PubMed]
15. Tian, X.; Cui, X.; Lai, T.; Ren, J.; Yang, Z.; Xiao, M.; Wang, B.; Xiao, X.; Wang, Y. Gas sensors based on TiO_2 nanostructured materials for the detection of hazardous gases: A review. *Nano Mater. Sci.* **2021**, *3*, 390–403. [CrossRef]
16. Deng, L.; Ding, X.; Zeng, D.; Zhang, S.; Xie, C. High sensitivity and selectivity of C-doped WO_3 gas sensors toward toluene and xylene. *IEEE Sens. J.* **2012**, *12*, 2209–2214. [CrossRef]

17. Kim, T.H.; Jeong, S.Y.; Moon, Y.K.; Lee, J.H. Dual-mode gas sensor for ultrasensitive and highly selective detection of xylene and toluene using Nb-doped NiO hollow spheres. *Sens. Actuators B Chem.* **2019**, *301*, 127140. [CrossRef]
18. Liang, Y.; Yang, Y.; Zou, C.; Xu, K.; Luo, X.; Luo, T.; Li, J.; Yang, Q.; Shi, P.; Yuan, C. 2D ultra-thin WO_3 nanosheets with dominant {002} crystal facets for high-performance xylene sensing and methyl orange photocatalytic degradation. *J. Alloys Compd.* **2019**, *783*, 848–854. [CrossRef]
19. Sheng, S.; Zhang, Z.; Wang, M.; He, X.; Jiang, C.; Wang, Y. Synthesis of MIL-125(Ti) derived TiO_2 for selective photoelectrochemical sensing and photocatalytic degradation of tetracycline. *Electrochim. Acta* **2022**, *420*, 140441. [CrossRef]
20. Adhikari, S.; Selvaraj, S.; Kim, D.H. Construction of heterojunction photoelectrode via atomic layer deposition of Fe_2O_3 on Bi_2WO_6 for highly efficient photoelectrochemical sensing and degradation of tetracycline. *Appl. Catal. B Environ.* **2019**, *244*, 11–24. [CrossRef]
21. Han, Q.; Zhao, X.; Na, N.; Ouyang, J. Integrating Near-Infrared Visual Fluorescence with a Photoelectrochemical Sensing System for Dual Readout Detection of Biomolecules. *Anal. Chem.* **2021**, *93*, 3486–3492. [CrossRef] [PubMed]
22. Li, Z.; Zhu, M. Detection of pollutants in water bodies: Electrochemical detection or photo-electrochemical detection? *Chem. Commun.* **2020**, *56*, 14541–14552. [CrossRef] [PubMed]
23. Najaf, Z.; Nguyen, D.L.T.; Chae, S.Y.; Joo, O.S.; Shah, A.U.H.A.; Vo, D.V.N.; Nguyen, V.-H.; Le, Q.V.; Rahman, G. Recent trends in development of hematite (α-Fe_2O_3) as an efficient photoanode for enhancement of photoelectrochemical hydrogen production by solar water splitting. *Int. J. Hydrog. Energy* **2021**, *46*, 23334–23357. [CrossRef]
24. Brillas, E.; Garcia-Segura, S. Recent progress of applied TiO_2 photoelectrocatalysis for the degradation of organic pollutants in wastewaters. *J. Environ. Chem. Eng.* **2023**, *11*, 109635. [CrossRef]
25. Bai, Z.; Yan, X.; Kang, Z.; Hu, Y.; Zhang, X.; Zhang, Y. Photoelectrochemical performance enhancement of ZnO photoanodes from $ZnIn_2S_4$ nanosheets coating. *Nano Energy* **2015**, *14*, 392–400. [CrossRef]
26. Raj, C.J.; Prabakar, K.; Karthick, S.N.; Hemalatha, K.V.; Son, M.K.; Kim, H.J. Banyan root structured Mg-Doped ZnO photoanode dye-sensitized solar cells. *J. Phys. Chem. C* **2013**, *117*, 2600–2607. [CrossRef]
27. Breuhaus-Alvarez, A.G.; Cheek, Q.; Cooper, J.J.; Maldonado, S.; Bartlett, B.M. Chloride Oxidation as an Alternative to the Oxygen-Evolution Reaction on H_xWO_3 Photoelectrodes. *J. Phys. Chem. C* **2021**, *125*, 8543–8550. [CrossRef]
28. Cao, X.; Zang, X.; Zhou, X.; Chen, M.; Ding, Y. Rationally designed/constructed MnO_x/WO_3 anode for photoelectrochemical water oxidation. *Chin. Chem. Lett.* **2018**, *29*, 811–814. [CrossRef]
29. Grigioni, I.; Ganzer, L.; VA Camargo, F.; Bozzini, B.; Cerullo, G.; Selli, E. In Operando Photoelectrochemical Femtosecond Transient Absorption Spectroscopy of WO_3/$BiVO_4$ Heterojunctions. *ACS Energy Lett.* **2019**, *4*, 2213–2219. [CrossRef]
30. Xia, L.; Bai, J.; Li, J.; Zeng, Q.; Li, L.; Zhou, B. High-performance $BiVO_4$ photoanodes cocatalyzed with an ultrathin α-Fe_2O_3 layer for photoelectrochemical application. *Appl. Catal. B Environ.* **2017**, *204*, 127–133. [CrossRef]
31. Rong, Y.Q.; Yang, X.F.; Zhang, W.D.; Yu, Y.X. Porous ultrathin WO_3 nanoflake arrays as highly efficient photoanode for water splitting. *Mater. Lett.* **2019**, *246*, 161–164. [CrossRef]
32. Lee, B.R.; Lee, M.G.; Park, H.; Lee, T.H.; Lee, S.A.; Bhat, S.S.M.; Kim, C.; Lee, S.; Jang, H.W. All-Solution-Processed WO_3/$BiVO_4$ Core-Shell Nanorod Arrays for Highly Stable Photoanodes. *ACS Appl. Mater. Interfaces* **2019**, *11*, 20004–20012. [CrossRef] [PubMed]
33. Petruleviciene, M.; Juodkazyte, J.; Parvin, M.; Tereschenko, A. Tuning the Photo-Luminescence Properties of WO_3 Layers by the Adjustment of Layer Formation Conditions. *Materials* **2020**, *13*, 2814. [CrossRef] [PubMed]
34. Petruleviciene, M.; Parvin, M.; Savickaja, I.; Gece, G.; Naujokaitis, A.; Pakstas, V.; Pilipavicius, J.; Gegeckas, A.; Gaigalas, G.; Juodkazyte, J. WO_3 coatings for photoelectrochemical synthesis of persulfate: Efficiency, stability and applicability. *J. Solid State Electrochem.* **2022**, *26*, 1021–1035. [CrossRef]
35. Petruleviciene, M.; Savickaja, I.; Juodkazyte, J.; Grinciene, G.; Ramanavicius, A. Investigation of $BiVO_4$-based advanced oxidation system for decomposition of organic compounds and production of reactive sulfate species. *Sci. Total Environ.* **2023**, *875*, 162574. [CrossRef] [PubMed]
36. Hill, J.C.; Choi, K.S. Effect of electrolytes on the selectivity and stability of n-type WO_3 photoelectrodes for use in solar water oxidation. *J. Phys. Chem. C* **2012**, *116*, 7612–7620. [CrossRef]
37. Petruleviciene, M.; Savickaja, I.; Griguceviciene, A.; Naujokaitis, A.; Ramanauskas, R.; Juodkazyte, J. Optimization of $BiVO_4$ coatings for high yield photoelectrochemical production of reactive chlorine species. *J. Photochem. Photobiol. A Chem.* **2023**, *443*, 114842. [CrossRef]
38. Parvin, M.; Petrulevičienė, M.; Savickaja, I.; Šebeka, B.; Karpicz, R.; Grigucevičienė, A.; Ramanauskas, R.; Juodkazytė, J. Influence of morphology on photoanodic behaviour of WO_3 films in chloride and sulphate electrolytes. *Electrochim. Acta* **2022**, *403*, 139710. [CrossRef]
39. Zheng, G.; Wang, J.; Liu, H.; Murugadoss, V.; Zu, G.; Che, H.; Lai, C.; Li, H.; Ding, T.; Gao, Q.; et al. Tungsten oxide nanostructures and nanocomposites for photoelectrochemical water splitting. *Nanoscale* **2019**, *11*, 18968–18994. [CrossRef]
40. Armstrong, D.A.; Huie, R.E.; Koppenol, W.H.; Lymar, S.V.; Merényi, G.; Neta, P.; Ruscic, B.; Stanbury, D.M.; Steenken, S.; Wardman, P. Standard electrode potentials involving radicals in aqueous solution: Inorganic radicals (IUPAC Technical Report). *Pure Appl. Chem.* **2015**, *87*, 1139–1150. [CrossRef]
41. Karlsson, R.K.B.; Cornell, A. Selectivity between Oxygen and Chlorine Evolution in the Chlor-Alkali and Chlorate Processes. *Chem. Rev.* **2016**, *116*, 2982–3028. [CrossRef] [PubMed]

42. Liang, C.; Huang, C.; Chen, Y. Potential for activated persulfate degradation of BTEX contamination. *Water Res.* **2008**, *42*, 4091–4100. [CrossRef] [PubMed]

43. Zeng, Y.; Guo, N.; Xu, X.; Yu, Y.; Wang, Q.; Wang, N.; Han, X.; Yu, H. Degradation of bisphenol a using peroxymonosulfate activated by $WO_3@MoS_2/Ag$ hollow nanotubes photocatalyst. *Chemosphere* **2019**, *227*, 589–597. [CrossRef]

44. Ye, Q.; Xu, H.; Zhang, J.; Wang, Q.; Zhou, P.; Wang, Y.; Huang, X.; Huo, X.; Liu, C.; Lu, J. Enhancement of peroxymonosulfate activation for antibiotics removal by nano zero valent tungsten induced Cu(II)/Cu(I) redox cycles. *Chem. Eng. J.* **2020**, *382*, 123054. [CrossRef]

45. Wang, Y.; Wang, D.; Dong, S.; Qiao, J.; Zeng, Z.; Shao, S. A visible-light-driven photoelectrochemical sensing platform based on the $BiVO_4/FeOOH$ photoanode for dopamine detection. *Electrochim. Acta* **2022**, *414*, 140207. [CrossRef]

46. Fukuzumi, S.; Ohkubo, K. Organic synthetic transformations using organic dyes as photoredox catalysts. *Org. Biomol. Chem.* **2014**, *12*, 6059–6071. [CrossRef]

47. Zeng, Q.; Wang, X.; Xie, X.; Mahmood, A.; Lu, G.; Wang, Y.; Sun, J. Band bending of TiO_2 induced by O-xylene and acetaldehyde adsorption and its effect on the generation of active radicals. *J. Colloid Interface Sci.* **2020**, *572*, 374–383. [CrossRef]

48. Mureithi, A.W.; Sun, Y.; Mani, T.; Howell, A.R.; Zhao, J. Impact of hole scavengers on photocatalytic reduction of nitrobenzene using cadmium sulfide quantum dots. *Cell Rep. Phys. Sci.* **2022**, *3*, 100889. [CrossRef]

49. Mesa, C.A.; Kafizas, A.; Francàs, L.; Pendlebury, S.R.; Pastor, E.; Ma, Y.; Le Formal, F.; Mayer, M.T.; Grätzel, M.; Durrant, J.R. Kinetics of Photoelectrochemical Oxidation of Methanol on Hematite Photoanodes. *J. Am. Chem. Soc.* **2017**, *139*, 11537–11543. [CrossRef]

50. Haisch, C.; Schneider, J.; Fleisch, M.; Gutzmann, H.; Klassen, T.; Bahnemann, D.W. Cold sprayed WO_3 and TiO_2 electrodes for photoelectrochemical water and methanol oxidation in renewable energy applications. *Dalt. Trans.* **2017**, *46*, 12811–12823. [CrossRef]

51. Wang, G.; Xie, X.; Cui, X.; Liu, J.; Jiang, L. Photoinduced $Pt/BiVO_4/Bi_2O_3$ Heterostructures for Methanol Oxidation and New Insights on the Photo-/Electrocatalysis Coupling Mechanism. *ACS Sustain. Chem. Eng.* **2021**, *9*, 4271–4281. [CrossRef]

52. Lutze, H.V.; Kerlin, N.; Schmidt, T.C. Sulfate radical-based water treatment in presence of chloride: Formation of chlorate, inter-conversion of sulfate radicals into hydroxyl radicals and influence of bicarbonate. *Water Res.* **2015**, *72*, 349–360. [CrossRef] [PubMed]

53. Monod, A.; Chebbi, A.; Durand-Jolibois, R.; Carlier, P. Oxidation of methanol by hydroxyl radicals in aqueous solution under simulated cloud droplet conditions. *Atmos. Environ.* **2000**, *34*, 5283–5294. [CrossRef]

54. Barroso, J.; Díez-Buitrago, B.; Saa, L.; Möller, M.; Briz, N.; Pavlov, V. Specific bioanalytical optical and photoelectrochemical assays for detection of methanol in alcoholic beverages. *Biosens. Bioelectron.* **2018**, *101*, 116–122. [CrossRef] [PubMed]

55. Ebrahim, Z. A Photoelectrochemical Sensor for Methanol based on Its Oxidation at TiO_2 Thin Film Modified Ti Electrode. *Anal. Bioanal. Electrochem.* **2019**, *11*, 566–576.

56. Alam, M.M.; Asiri, A.M.; Uddin, M.T.; Rahman, M.M.; Islam, M.A. An alternative electrochemical approach for toluene detection with $ZnO/MgO/Cr_2O_3$ nanofibers on a glassy carbon electrode for environmental monitoring. *RSC Adv.* **2020**, *10*, 44641–44653. [CrossRef]

57. Garcia de Freitas Junior, G.; Florêncio, T.M.; Mendonça, R.J.; Salazar-Banda, G.R.; Oliveira, R.T.S. Simultaneous Voltammetric Determination of Benzene, Toluene and Xylenes. *Electroanalysis* **2019**, *31*, 554–559. [CrossRef]

58. Rao, Y.F.; Chu, W.; Wang, Y.R. Photocatalytic oxidation of carbamazepine in triclinic-WO_3 suspension: Role of alcohol and sulfate radicals in the degradation pathway. *Appl. Catal. A Gen.* **2013**, *468*, 240–249. [CrossRef]

59. Ahmed, N.; Vione, D.; Rivoira, L.; Carena, L.; Castiglioni, M.; Bruzzoniti, M.C. A review on the degradation of pollutants by fenton-like systems based on zero-valent iron and persulfate: Effects of reduction potentials, ph, and anions occurring in waste waters. *Molecules* **2021**, *26*, 4584. [CrossRef]

60. Ganiyu, S.O.; Gamal El-Din, M. Insight into in-situ radical and non-radical oxidative degradation of organic compounds in complex real matrix during electrooxidation with boron doped diamond electrode: A case study of oil sands process water treatment. *Appl. Catal. B Environ.* **2020**, *279*, 119366. [CrossRef]

61. Wojnárovits, L.; Takács, E. Rate constants of sulfate radical anion reactions with organic molecules: A review. *Chemosphere* **2019**, *220*, 1014–1032. [CrossRef] [PubMed]

62. Xiao, R.; Ye, T.; Wei, Z.; Luo, S.; Yang, Z.; Spinney, R. Quantitative Structure-Activity Relationship (QSAR) for the Oxidation of Trace Organic Contaminants by Sulfate Radical. *Environ. Sci. Technol.* **2015**, *49*, 13394–13402. [CrossRef] [PubMed]

63. Xin, S.; Ma, X.; Lu, J.; Zhang, G.; Huo, S.; Gao, M.; Xu, P.; Liu, W. Enhanced visible light photoelectrocatalytic degradation of o-chloronitrobenzene through surface plasmonic Au nanoparticles and g-C_3N_4 co-modified TiO_2 nanotube arrays photoanode. *Appl. Catal. B Environ.* **2023**, *323*, 122174. [CrossRef]

64. Shen, Z.; Zhang, Y.; Zhou, C.; Bai, J.; Chen, S.; Li, J.; Wang, J.; Guan, X.; Rahim, M.; Zhou, B. Exhaustive denitrification via chlorine oxide radical reactions for urea based on a novel photoelectrochemical cell. *Water Res.* **2020**, *170*, 115357. [CrossRef] [PubMed]

65. Cristino, V.; Pasti, L.; Marchetti, N.; Berardi, S.; Bignozzi, C.A.; Molinari, A.; Passabi, F.; Caramori, S.; Amidani, L.; Orlandi, M.; et al. Photoelectrocatalytic degradation of emerging contaminants at $WO_3/BiVO_4$ photoanodes in aqueous solution. *Photochem. Photobiol. Sci.* **2019**, *18*, 2150–2163. [CrossRef]

66. Liu, C.; Mao, S.; Wang, H.; Wu, Y.; Wang, F.; Xia, M.; Chen, Q. Peroxymonosulfate-assisted for facilitating photocatalytic degradation performance of 2D/2D $WO_3/BiOBr$ S-scheme heterojunction. *Chem. Eng. J.* **2022**, *430*, 132806. [CrossRef]

67. Rabé, K.; Liu, L.; Nahyoon, N.A.; Zhang, Y.; Idris, A.M. Enhanced Rhodamine B and coking wastewater degradation and simultaneous electricity generation via anodic g-C_3N_4/Fe 0 (1%)/TiO_2 and cathodic WO_3 in photocatalytic fuel cell system under visible light irradiation. *Electrochim. Acta* **2019**, *298*, 430–439. [CrossRef]
68. Longobucco, G.; Pasti, L.; Molinari, A.; Marchetti, N.; Caramori, S.; Cristino, V.; Boaretto, R.; Bignozzi, C.A. Photoelectrochemical mineralization of emerging contaminants at porous WO_3 interfaces. *Appl. Catal. B Environ.* **2017**, *204*, 273–282. [CrossRef]
69. Sun, B.; Li, H.; Wei, Q.; Xue, S.; Zhou, A.; Yue, X. Enhanced quinoline degradation by persulfate-assisted photocatalytic process with WO_3-$CuFe_2O_4$ Z-scheme system: Properties and mechanism. *Sep. Purif. Technol.* **2022**, *301*, 122039. [CrossRef]